Structure, mechanical characteristics, oxidation and cavitation resistance of Fe–Cr–Al based alloys

I.V.Kolodiy, V.A.Belous, M.A.Bortnitskaya, R.L.Vasilenko, V.N.Voyevodin, V.I.Kovalenko, A.S.Kuprin, V.G.Marinin, V.D.Ovcharenko, G.Y.Rostova, P.I.Stoev, M.A.Tikhonovsky, G.N.Tolmachova, A.S.Tortika

National Science Center "Kharkiv Institute of Physics and Technology", 1 Academichna Str., 61108 Kharkiv, Ukraine

Fe–Cr–Al alloys are considered as one of the possible replacement of zirconium alloys for nuclear fuel claddings. The microstructure, phase composition, oxidation resistance, mechanical properties and cavitation resistance of one commercial and four experimental Fe–Cr–Al alloys doped with yttrium, molybdenum and zirconium are studied in this work. All alloys under study have the BCC phase as the main. Alloying with ~ 2 % of zirconium results in the formation of microstructure consisting of the matrix phase grains and intergranular eutectic: BCC matrix phase + FCC Laves phase $ZrFe_2$. The highest resistance to oxidation in air at temperature of 1300°C is observed in the alloy doped with yttrium and molybdenum. Microhardness, nanohardness and yield strength have close values for all alloys except for the Zr-doped alloy which has significantly higher values of these parameters. The Fe–Cr–Al alloy doped by Y, Mo and Zr is the most cavitation resistant one.

Keywords: Fe–Cr–Al alloy, structure, oxidation resistance, cavitation, phase composition.

Сплавы на основе Fe–Cr–Al рассматриваются, как один из возможных вариантов замены циркониевых сплавов для оболочек ядерного топлива. Исследованы микроструктура, фазовый состав, стойкость к окислению, механические свойства и кавитационная стойкость промышленного и четырех экспериментальных сплавов на основе системы Fe–Cr–Al, легированных иттрием, молибденом и цирконием. Основу всех исследованных сплавов составляет ОЦК фаза. Легирование ~ 2 % циркония приводит к формированию в сплаве микроструктуры, состоящей из зерен матричной ОЦК фазы и межзеренной эвтектики — ОЦК матричная фаза + ГЦК фаза Лавеса $ZrFe_2$. Наибольшей стойкостью к окислению на воздухе при температуре 1300°C обладает сплав, легированный иттрием и молибденом. Микротвердость, нанотвердость и предел текучести на сжатие для сплавов близки, за исключением сплава, легированного цирконием, у которого эти характеристики существенно выше. Наиболее стойким к воздействию кавитации является сплав Fe–Cr–Al легированный Y, Mo и Zr.

Структура, механічні характеристики, стійкість до окислення та кавітації сплавів на основі Fe–Cr–Al. *І.В.Колодій, В.А.Білоус, М.О.Бортницька, Р.Л.Василенко, В.М.Воєводін, В.І.Коваленко, О.С.Купрін, В.Г.Марінін, В.Д.Овчаренко, Г.Ю.Ростова, П.І.Стоєв, М.А.Тихоновський, Г.М.Толмачова, О.С.Тортіка.*

Сплави на основі Fe–Cr–Al розглядаються як один з можливих варіантів заміни цирконієвих сплавів для оболонок ядерного палива. Досліджено мікроструктуру, фазовий склад, стійкість до окислення, механічні властивості та кавітаційну стійкість промислового і чотирьох експериментальних сплавів на основі системи Fe–Cr–Al, легованих ітрієм,

молібденом і цирконієм. Основу всіх досліджених сплавів становить ОЦК фаза. Легування ~ 2 % цирконію призводить до формування у сплаві мікроструктури, що складається з зерен матричної ОЦК фази і міжзеренної евтектики — ОЦК матрична фаза + ГЦК фаза Лавеса $ZrFe_2$. Найбільшу стійкість до окислення на повітрі при температурі 1300°C має сплав, легований ітрієм і молібденом. Мікротвердість, нанотвердість і межа плинності на стиснення для сплавів близькі, за винятком сплаву, легованого цирконієм, у якого ці показники значно вище. Найбільш стійким до впливу кавітації є сплав Fe–Cr–Al легований Y, Mo і Zr.

1. Introduction

After the Fukushima nuclear power plant accident (March 11, 2011), Fe–Cr–Al-based alloys are considered within the ATFC concept as one of the possible materials for replacing traditional zirconium alloys for fuel claddings [1, 2]. These alloys have improved oxidation resistance (reduced hydrogen generation) and higher strength compared to existing Zr-based alloys, at least up to a temperature of 1300°C. Both of these properties are necessary to increase the fuel stability to accident situations and might facilitate for increasing the response time in the accident with loss of coolant (LOCA condition) [3]. Specific features of the Fe–Cr–Al-based alloys are the formation of a thin alumina protective film at high-temperature tests in water vapor [4] and high corrosion resistance under close to normal operation conditions due to the formation of a spinel film of chromium and iron oxides [5]. Once more advantage of these alloys, in comparison to the corrosion-resistant austenitic steels, is the absence of nickel, which is undesirable element in materials for thermal neutron reactors [6]. These alloys also satisfy the requirements for fuel cladding materials by the complex of neutron-physical characteristics and radiation resistance [7, 8]. Also, the Fe–Cr–Al-based alloys can be used as a protective coating on zirconium-based fuel claddings [9]. In normal reactor operation conditions, the fuel claddings are also undergo different types of mechanical wear (abrasion and micro-shock damage) which can lead to violation of their integrity and radioactive products leakage [10–12]. Mechanical wear resistance of the material depends on composition, structural-phase state and physical-mechanical properties. It was experimentally shown [11] that the wear resistance of the Fe–Cr–Al alloy is comparable to that of a zirconium-based alloy. But no data on the micro-shock resistance (cavitation) of Fe–Cr–Al and Zr-based alloys are known to the authors.

The aim of this work is to study the influence of doping elements (Y, Mo, and Zr) on the structure, oxidation resistance, and physical-mechanical properties of the Fe–Cr–Al-based alloys.

2. Experimental

Six alloys were selected as materials for the study (No.1–6); two of them (No. 1, 2) were commercial alloys Kanthal A1:

1) No. 1 — Kanthal A1 (commercial alloy);
2) No. 2 — remelted Kanthal A1 alloy;
3) No. 3 — 72.5Fe–21Cr–6Al–0.5Y;
4) No. 4 — 72Fe–21Cr–6Al–1Y;
5) No. 5 — 70Fe–21Cr–6Al–1Y–2Mo;
6) No. 6 — 63Fe–Cr–9Al–1Y–2Mo–2Zr.

The sample No. 1 (a round bar of 20 mm in diameter) was in the initial (as delivered) state; the sample No. 2 was the similar rod remelted by the argon-arc method and casted into a cylindrical copper mold of 10 mm in diameter. The experimental alloys No. 3–6 were melted under the same conditions. High purity metals were used as the raw materials (armco iron, aluminum 99.99 %, electrolytic chromium 99.99 %, molybdenum 99.9 %, zirconium 99.9 %, and metallic yttrium 99 %). At least five melting with turning over at each remelting were performed to improve the chemical homogeneity of the ingots. The final solidified ingots were cylindrical bars with a diameter of 10 mm and height of 30 mm, weighing $\approx$ 30 grams.

The density of the samples was measured pycnometrically. Microstructure was characterized using a scanning electron microscope JSM-7001F equipped with an Oxford Link ISIS 300 EDX attachment. The crystalline structure and phase composition were studied using an X-Ray diffractometer DRON-2.0 with Co–Kα radiation and a Fe selective filter.

The effect of alloys composition on their high-temperature oxidation resistance was studied by annealing in a furnace in air at atmospheric pressure and a temperature of $T = 1300$°C for 3 h. After oxidation, the samples were weighted with laboratory scales VLR-20 with an accuracy of ±0.015 mg.

The microhardness of the alloys was measured using a Leco LM700AT microhardness tester with a Vickers diamond in-

Table 1. Chemical composition of alloys

Sample No.	Concentration, wt %					
	Fe	Cr	Al	Other elements		
1 (initial bar)	bal.	22.65	4.04	Si — 0.53	Ti — 0.21	Mn — 0.28 Ni — 0.13
2 (ingot)	bal.	22.52	4.06	Si — 0.58	Ti — 0.22	Mn — 0.29
3 (ingot)	72.34	21.85	5.68	Y — 0.13		
4 (ingot)	71.26	21.84	6.07	Y — 0.83		
5 (ingot)	69.72	21.82	5.35	Y — 0.53	Mo — 2.58	
6 (ingot)	62.99	23.86	8.55	Y — 0.66	Mo — 2.07	Zr — 1.87

denter under a load of 200 g. Nano-hardness and Young's modulus of the alloys were measured according to the Oliver and Pharr method [13] with a Nano Indenter G200 instrument (Agilent Technologies) with a Berkovich diamond indenter at the penetration depth of 200 nm. Compressive yield strength (σ_T) measurements were carried out using a universal testing machine 1958 U10-1 with a deformation rate of 0.17 mm/min at room temperature.

To obtain data on the strength characteristics of the alloys under microshock loading, the cavitation surface loading method (ASTM G32 standard) was used. In this case, the surface of the samples under the influence of cavitating voids is subjected to high loading rates localized in small areas, and high repeatability of the results is ensured. The resulting stresses can be comparable with the tensile strength of the material, and concentrated in areas close to the dimensions of structural components. A stand developed at NSC KIPT [14] was used in the experiments to determine the cavitation resistance of the alloys. In this stand, a cavitation zone was formed under the end of the exponential ultrasonic emitter (frequency $f = 21\pm1$ kHz, magnitude is 30 ± 1 μm) in distilled water over the surface of the sample. Mass loss of the samples after the cavitation exposure was measured with the laboratory scale VLR-20 with an accuracy of ±0.015 mg.

The experimental data were presented in the form of kinetic curves, which are characterized by the presence of two areas: the initial area, when the fracture is small, and the area with the maximum quasi-constant speed. From the kinetic curves, the average mass destruction rates (V_S) of the alloys were determined.

3. Results and discussion

3.1 Microstructure and chemical composition of alloys

Chemical composition of the alloys was determined by EDX analysis as shown in Table 1. The measured composition of the Kanthal A1 alloy (for the samples No. 1, 2) was compared to GOST 10994-74 data [15].

Analysis of the data presented in Table 1 allows making the following conclusions:

– Element concentrations in the commercial alloy comply with GOST, except for aluminum which amount are noticeably lower than the GOST requirements.

– The composition of the bars after the arc remelting the commercial alloy remains practically unchanged.

– After melting the raw metals, a reduced concentration of aluminum and yttrium is observed in the ingots compared to the nominal composition (except for the sample No. 3). This may be due to the transition of these elements into slag after multiple remelting as a result of their interaction with residual oxygen.

A slight excess of the chromium concentration in the ingots No. 3–6 is a consequence of the fact that the amount of metallic chromium was calculated higher than nominal (by about 0.5 %) taking into account its evaporation; as well, the concentrations of aluminum and yttrium decrease as noted above. It should be noted that element concentrations in Table 1 were determined by scanning over a sufficiently large area (about 1 mm²). Microstructure analysis and chemical analysis at individual "points" (size of 5–10 μm²) showed that aluminum, chromium, silicon, manganese, nickel and molybdenum were fairly uniform distributed in the main matrix phase. In other words, these elements form substitutional solid solutions with iron; this is consistent
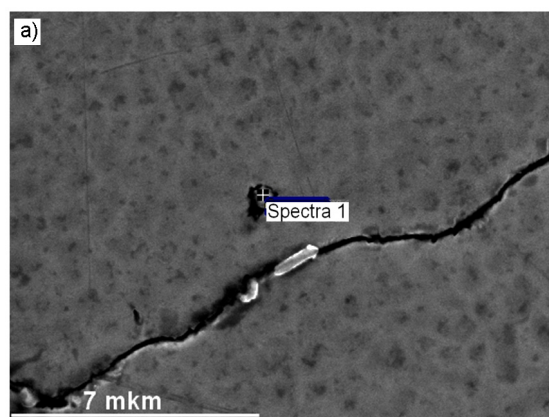
Element	Concentration	
	wt.%	at.%
Al	3.60	6.81
Si	0.63	1.14
P	1.54	2.53
Ti	12.60	13.43
Cr	21.89	21.48
Fe	59.75	54.60

Fig. 1. Image (a) and chemical composition (b) of titanium-containing precipitation in sample No. 1.

Fig. 2. Microstructure of commercial Kanthal A1 alloy: a — initial (No. 1); b — after remelting (No. 2).

with the known phase diagrams of iron-based binary systems [16].

At the same time, titanium in the commercial alloys (samples No. 1, 2) is distributed very unevenly. The matrix phase contains 2–3 times less titanium (0.06–0.13 %) than in the whole sample. The rest amount of the titanium is concentrated in precipitations (Fig. 1) which also contain a significant amount of phosphorus. It should be noted that the precipitation sizes are significantly smaller than the size of the zone excited by the electron beam; therefore, the composition of the precipitations is determined qualitatively. Apparently, the binding of titanium with phosphorus which is usually located at grain boundaries in the concentration up to 0.03 % in Kanthal A1 alloy, has a positive effect on mechanical properties of the alloy. The microstructure of the commercial alloy is typical for a recrystallized material with a grain size ≥ 100 μm (Fig. 2a). The ingot from this alloy has approximately the same microstructure (Fig. 2b), but with a larger grain size (up to 1 mm).

The samples (ingots) No. 3–5 have an anisotropic coarse-grained microstructure (grain size near several mm), wherein the grains are elongated in the direction of heat sink. The yttrium distribution in the ingots is of 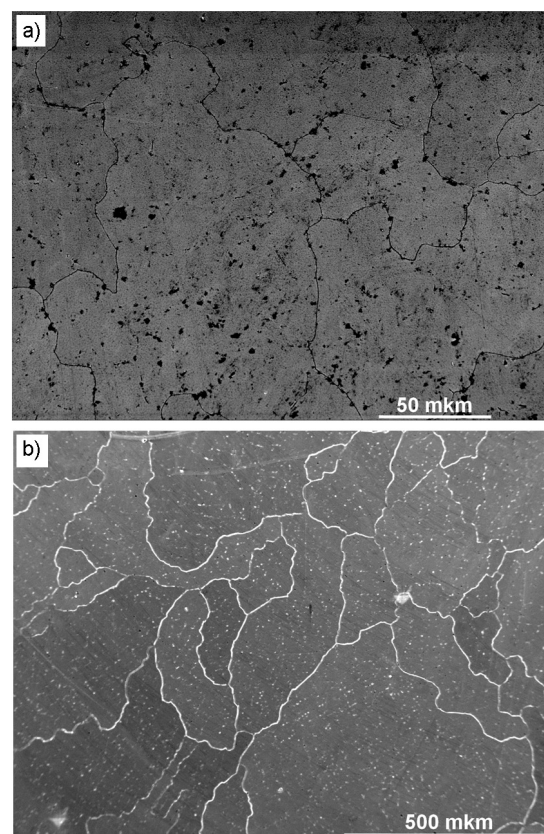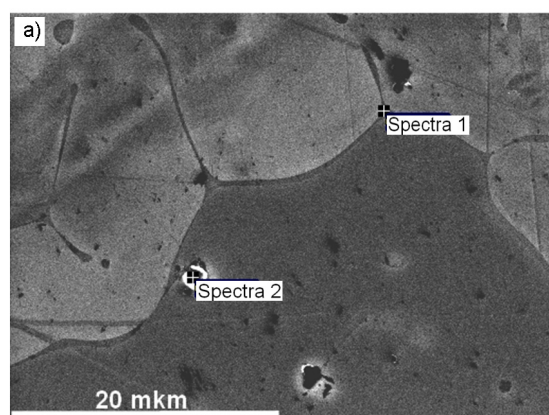greatest interest. Microanalysis showed that there is no yttrium in the grains body of the matrix phase (its concentration is less than the detection limit of about 0.1 at %). The main amount of yttrium is concentrated at grain boundaries or in precipitations (Fig. 3a). These precipitations are yttrium oxides (Fig. 3b, spectrum 2). This yttrium distribution is due to its low solubility in iron and, as a consequence, in the matrix phase [16].

A significant change in the microstructure is observed in the sample No. 6 (Zr doped). Firstly, grain refinement takes place; and secondly, the eutectic component appears at the grain boundaries (Fig. 4). As in the case of yttrium, the concentration of zirconium in the matrix phase is below the detection limit due to its low solubility in iron [16]. The zirconium concentration in the eutectic is 15.2±1.2 % (average value over several measurements), which is close to eutectic concentration in a binary system Fe–Zr [17]. Average values of other element concentrations in the eutectic are: 9.0±0.3 % of Al, 13.9±0.16 % of Cr, 4.96±0.45 % of Y, and 1.5±0.05 % of Mo.

Fig. 3. Microstructure of the alloy No. 4 (a), element concentrations at grain boundaries (b, Spectrum 1) and composition of oxide precipitation (b, Spectrum 2).

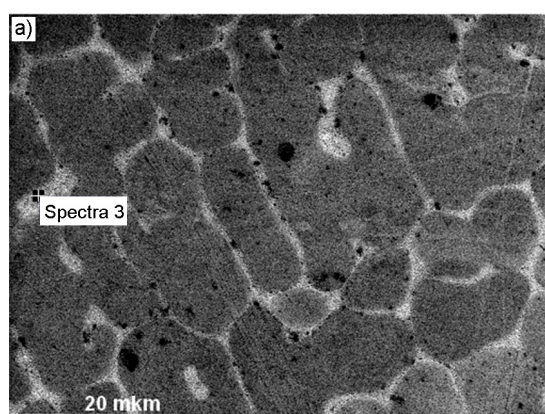| Element	Concentration			
	Spectra 1		Spectra 2	
	wt.%	at.%	wt.%	at.%
Al	7.18	14.29	2.14	3.52
Cr	15.47	15.97	7.77	6.64
Fe	64.41	61.92	25.53	20.33
Y	12.95	7.82	48.23	24.12
O	-	-	16.33	45.39
Summary	100		100	

Thus, almost all Zr and Y are concentrated in the eutectic; Cr is near uniformly distributed between the matrix phase and eutectic, although its concentration in the eutectic is 2 times lower than in the matrix phase.

3.2. Phase composition and crystal structure of alloys

According to XRD analysis (Fig. 5a, Table 2), the samples No. 1−5 are single-phase BCC alloys (within the detection limit). The lattice parameter of the BCC phase increases with increasing the content of doping elements. There is an additional peak on the diffraction pattern of the sample No. 6, which, most likely, corresponds

Table 2. Phase composition and lattice parameters of phases in samples No.1−No.6

No.	Phase	Lattice parameters, Å
1	BCC	2.8832
2	BCC	2.8835
3	BCC	2.8871
4	BCC	2.8897
5	BCC	2.8914
6	BCC	2.8966
	$ZrFe_2$	7.03

Element	Concentration	
	wt.%	at.%
Al	9.35	18.80
Cr	13.77	14.37
Fe	55.82	54.25
Y	5.50	3.36
Zr	14.09	8.38
Mo	1.47	0.83
Summary	100.00	

Fig. 4. Microstructure (a) and chemical composition of intergranular eutectic (b) in sample No. 6.
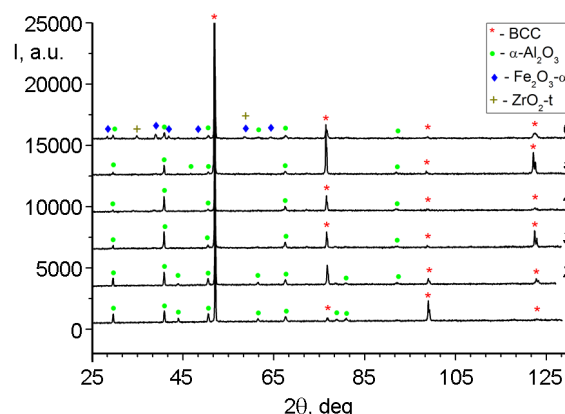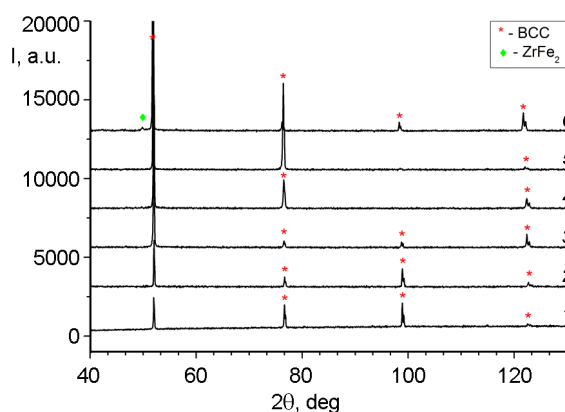

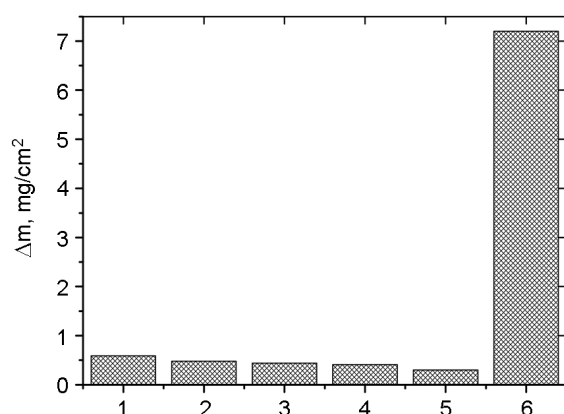Fig. 5. Diffraction patterns of Fe−Cr−Al alloys before (a) and after (b) air oxidation at $T = 1300°C$ for 3 h.

Fig. 6. The mass gains in Fe–Cr–Al samples after oxidation in air at $T = 1300°C$ for 3 h.

to ZrFe$_2$ Laves phase. This is consistent with the Fe–Zr phase diagram where ZrFe$_2$ is the second phase in the iron-rich eutectic.

3.3. High-temperature oxidation resistance

The test results on high-temperature ($T = 1300°C$) oxidation resistance of the samples are shown in Fig. 6.

After the high-temperature tests, the samples of all compositions showed the mass gain without shedding (peeling) of a dense dark-gray oxide film. The lowest mass gain (0.3 mg/cm^2) was observed for the samples doped by molybdenum, and the highest gain (7.2 mg/cm^2) — for the samples doped by zirconium. This behavior of the alloys during oxidation is a result of the formation of oxide layers with different phase compositions on their surface (Fig. 5b). In the diffraction patterns of all the samples after oxidation, the BCC phase and alumina Al$_2$O$_3$–α were identified (Fig. 5b, Table 3).

Lattice parameters of the BCC phase after oxidation are slightly less than in the

Table 3. Phase composition of surface layers of samples after oxidation

No	Phase	Lattice parameters, Å
1	BCC	2.8809
	Al$_2$O$_3$–α	$a = 4.780$, $c = 13.034$
2	BCC	2.8812
	Al$_2$O$_3$–α	$a = 4.787$, $c = 13.037$
3	BCC	2.8869
	Al$_2$O$_3$–α	$a = 4.796$, $c = 13.040$
4	BCC	2.8877
	Al$_2$O$_3$–α	$a = 4.789$, $c = 13.053$
5	BCC	2.8909
	Al$_2$O$_3$–α	$a = 4.796$, $c = 13.032$
6	BCC	2.8896
	Al$_2$O$_3$–α	$a = 4.784$, $c = 13.055$
	Fe$_2$O$_3$–α	$a = 5.007$, $c = 13.669$
	ZrO$_2$–t	$a = 3.64$, $c = 5.25$

initial state, however, a tendency to increase with increasing the doping elements content is observed. The decrease in the lattice parameters of the BCC phase is probably due to the decrease in the aluminum concentration in the surface layer as a result of its transition to alumina. The lowest high-temperature oxidation resistance is found in the sample No. 6. The diffraction pattern of this sample clearly shows the presence of iron oxide Fe$_2$O$_3$–α and tetragonal zirconia ZrO$_2$–t along with above phases.

3.4. Mechanical properties of alloys

Data on mechanical properties of the investigated alloys are given in Table 4. It can be seen that doping the Fe–Cr–Al alloy with various chemical elements changes its mechanical and wear-resistant properties.

Table 4. Mechanical properties of Fe–Cr–Al-based alloys (ρ is density, H is nano-hardness, E is Young's modulus, H_μ^{200} is microhardness with a load of 200 g, σ$_T$ is compressive yield strength, V_S is speed of cavitation damage)

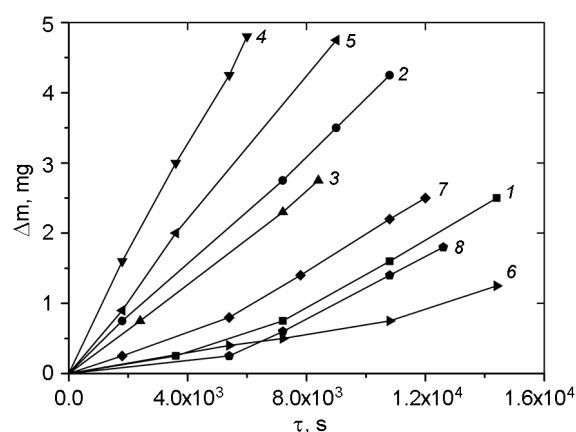| Sample	Mechanical properties							
	ρ, g/cm^3	H, GPa	E, GPa	H/E	H^3/E^2, GPa	H_μ^{200}, GPa	σ$_T$, kg/mm^2	V_S·10^2, mm^3/h
1	6.8	3.6	230.6	0.016	8.8·10^{-4}	2.35	60.2	9.7
2	7.13	3.7	218.7	0.017	1.1·10^{-3}	2.40	53.4	19.6
3	7.2	3.3	220.6	0.015	7.4·10^{-4}	2.22	44.2	18.8
4	6.82	3.4	217.5	0.016	8.3·10^{-4}	2.45	55.7	–
5	6.93	3.7	219.4	0.017	1.1·10^{-3}	2.51	54.5	27.3
6	6.56	4.9	215.6	0.023	2.5·10^{-3}	3.42	97.6	4.57

Fig. 7. Mass loss versus time of cavitation effect. *1–6* are the samples numbers in Table 1; *7* – Zr–1Nb, *8* — Zr–2.5Nb.

Parameters H/E and H^3/E^2 are used to assess the wear-resistance and plastic deformation resistance of the materials, respectively [18, 19].

Nano-hardness, Young's modulus, microhardness and compressive yield strength are reduced for alloys, doped only by Y (No. 3, 4). Additional Mo doping (sample No. 5) leads to increasing nano-hardness and microhardness. Simultaneous Y, Mo, and Zr doping (No. 6) results in increase of all the mechanical properties of the alloy; moreover, in this case, the H/E and H^3/E^2 parameters are the highest for all the studied samples.

Kinetic curves of cavitation damage of the studied Fe–Cr–Al alloys in comparison with Zr–1Nb and Zr–2.5Nb zirconium alloys are shown in Fig. 7.

Analysis of the data presented in Fig. 7 shows that the sample No. 6 (doped by Y, Mo and Zr) is the most resistant to microshock loading under cavitation. The average rate of its destruction is 2.5 and 1.9 times less than that among Zr–1Nb and Zr–2.5Nb zirconium alloys, respectively.

4. Conclusions

The microstructure, phase composition, oxidation resistance, mechanical properties and cavitation resistance of commercial and four experimental Fe–Cr–Al-based alloys doped by Y, Mo and Zr were investigated. The research results suggest the following conclusions:

– The main phase in the commercial Kanthal A1 alloy and experimental alloys is the BCC phase (substitutional solid solution). Silicon, manganese, and nickel, observed in the commercial alloy, are uniformly distrib-uted in the BCC phase. Molybdenum doped into the experimental Fe–Cr–Al alloys in amount of 2 % behaves in the same way. At the same time, titanium in the commercial alloy is distributed very unevenly. The matrix BCC phase contains 2–3 times less titanium (0.06–0.13 %) than the whole sample. The rest amount of titanium is concentrated in precipitations which also contain a significant amount of phosphorus. A similar non-uniform distribution is observed for yttrium in the solid solution which contains no more than 0.1 % yttrium. The rest amount of yttrium is concentrated at grain boundaries and oxide precipitations. In this case yttrium doping leads to a noticeable grain refinement of the as-cast alloys.

– Doping with ~ 2 % Zr results in the formation of microstructure which consists of the matrix phase grains and intergranular eutectic: BCC matrix phase + FCC Laves phase $ZrFe_2$. The main amount of yttrium and zirconium is concentrated in the eutectic (probably in the Laves phase).

– The highest resistance to oxidation in air at 1300°C is observed in the alloy with the Fe–21 %Cr–6 %Al–1 %Y–2 %Mo composition. Corrosion resistance sharply decreases upon doping with zirconium, apparently, as a result of the formation of iron oxide Fe_2O_3–α and zirconium oxide ZrO_2–t in the surface, in addition to alumina Al_2O_3–α, layer, which is characteristic for all alloys.

– Values of microhardness, nano-hardness and compressive yield strength are similar for all the alloys, except for the Zr doped alloy for which these values are significantly higher.

– Cavitation resistance of studied alloys is highly dependent on alloying elements. The most resistant to microshock loading under cavitation is alloy, doped by Y, Mo and Zr.

– Since the strength characteristics of the Fe–Cr–Al-based alloys are no worse than those of zirconium alloys, the most important characteristic for using these alloys as reactor materials is their resistance to high temperature oxidation. Proceeding from this alloy No. 5 (doped with Y and Mo) is the most promising alloy among all studied in this research.

References

1. K.A.Terrani. *J. Nucl. Mater.*, **501**, 13 (2018).
2. Z.Duan, H.Yang, Y.Satoh et al., *Nucl. Eng. Des.*, **316**, 131 (2017).
3. K.A.Terrani, S.J.Zinkle, L.L.Snead, *J. Nucl. Mater.*, **448**, 420 (2014).

4. B.A.Pint, K.A.Terrani, M.P.Brady et al., *J. Nucl. Mater.*, **440**, 420 (2013).

5. K.A.Terrani, B.A.Pint, K.A.Unocic et al., *J. Nucl. Mater.*, **479**, 36 (2016).

6. B.A.Pint, K.A.Terrani, Y.Yamamoto, L.L.Snead, *Metall. Mater. Trans. E*, **2**, 190 (2015).

7. X.Wu, T.Kozlowski, J.D.Hales, *Ann. Nucl. Energy*, **85**, 763 (2015).

8. K.G.Field, X.Hu, K.C.Littrell et al., *J. Nucl. Mater.*, **465**, 746 (2015).

9. Y.Wang, W.Zhou, Q.Wen et al., *Surf. Coat. Tech.*, **344**, 141 (2018).

10. Hyung-Kyu Kim, Young-Ho Lee, Sung-Pil Heo, *Tribol. Int.*, **39**, 1305 (2006).

11. Young-Ho Lee, Thak Sang Byun, *J. Nucl. Mater.*, **465**, 857 (2015).

12. K.Edsinger, *The Nuclear News*, 40 (2010).

13. W.C.Oliver, G.M.Pharr, *J. Mater. Res.*, **7**, 1564 (1992).

14. V.G.Marinin, V.I.Kovalenko, N.S.Lomino et al., in: Proc. Intern. Symposium on Discharges and Electrical Insulation in Vacuum, ISDEIV, v. 2, (2000), p.567.

15. GOST 10994-74. Precision Alloys. Grades [in Russian].

16. O.A.Bannych, P.B.Bydberg, S.P.Alisova et al., Phase Diagrams of Binary and Multicomponent Fe-based Systems, Metallurgy (1986) [in Russian].

17. V.V.Reznichenko, A.I.Somov, M.A.Tikhonovsky, *Phys. Met. Metallogr.*, **37**, 657 (1973).

18. A.Leyland, A.Matthews, *Wear*, **246**, 1 (2000).

19. J.Musil, F.Kunc, H.Zeman, H.Polakova, *Surf. Coat. Technol.*, **54**, 304 (2002).